Special Feature: Tutorial

Journal of MASS SPECTROMETRY

Received: 27 October 2009 Accepted: 11 February 2010 Published online in Wiley Interscience: 18 March 2010

(www.interscience.com) DOI 10.1002/jms.1732

Molecular dynamics simulations of MALDI: laser fluence and pulse width dependence of plume characteristics and consequences for matrix and analyte ionization

Richard Knochenmuss[a]* and Leonid V. Zhigilei[b]

Molecular dynamics simulations of matrix-assisted laser desorption/ionization were carried out to investigate laser pulse width and fluence effects on primary and secondary ionization process. At the same fluence, short (35 or 350 ps) pulses lead to much higher initial pressures and ion concentrations than longer ones (3 ns), but these differences do not persist because the system relaxes toward local thermal equilibrium on a nanosecond timescale. Higher fluences accentuate the initial disparities, but downstream differences are not substantial. Axial velocities of ions and neutrals are found to span a wide range, and be fluence dependent. Total ion yield is only weakly dependent on pulse width, and consistent with experimental estimates. Secondary reactions of matrix cations with analyte neutrals are efficient even though analyte ions are ablated in clusters of matrix. Copyright © 2010 John Wiley & Sons, Ltd.

Keywords: MALDI; ionization; ablation; molecular dynamics; ion velocities

Introduction

Matrix-assisted laser desorption/ionization (MALDI) is a complex process, involving a variety of physical and chemical phenomena, over widely different time scales.[1–3] In addition, the two main variants of MALDI, using ultraviolet (UV) or infrared laser excitation, may involve significantly different ionization mechanisms.

Energy is deposited quickly in MALDI, typically on a nanosecond or faster time scale, but expansion of the ablated material until ions are freely extractable may take microseconds. Because of this difference, it is useful to distinguish between primary ionization events occurring during or shortly after the laser pulse, and subsequent secondary ion–ion and ion–molecule reactions in the expanding plume. The greatest difficulties in understanding MALDI lie in the primary mechanisms, the secondary plume reactions are believed to be well described by gas-phase ion-molecule reaction thermodynamics and kinetics.[1]

Numerous possible UV primary ionization mechanisms have been reviewed in detail.[1] The two-step pooling model used here has been elaborated for the matrix 2,5-dihydroxybenzoic acid (DHB), but may apply to others as well.[4,5] In this model energy deposited by the laser in the excited states of a matrix molecule is able to migrate in the solid as a pseudo-particle (exciton). When two such excitons meet, their collective energy can be concentrated on a single matrix molecule, a process known as pooling. A high energy exciton can pool with another exciton to create an ion-electron pair. The electron is captured by another matrix molecule (unless the event is near the surface) resulting in a complementary pair of matrix ions. These ions may react further with other matrix or analyte molecules in secondary processes, which lead to the ions that are finally observed.

These processes have been quantitatively characterized for DHB, and a differential equation model was developed to predict both matrix and analyte ion yields.[4–6] A key aspect of the model is that it explicitly couples the ionization reactions to the plume expansion, via the reaction kinetics. Since primary pooling, collisional deactivation, secondary ion–ion and ion–molecule reactions are all bimolecular, local pressure and temperature strongly modulate reaction rates. In particular, rates rapidly decrease as the plume expands, until they effectively stop. The plume never reaches a true equilibrium state, which is fortunate for mass spectrometry. It is only because of this that recombination of positive and negative charge is incomplete, leaving some ions available for mass analysis.

The model has proven successful in reproducing a wide variety of MALDI phenomena, in a quantitative or semi-quantitative manner. At the same time, it has known limitations. It assumes that the ablated sample becomes a uniform molecular gas at a fixed temperature, and also assumes an ideal supersonic expansion of the gas after the phase transition. As demonstrated in molecular dynamics (MD) simulations of references [7–14] the ablation event induced by the laser irradiation is more complex and results in ejection of a mixture of individual molecules and molecular clusters/droplets of different sizes. This is consistent with experiments that show significant portion of the ablated material may be in the form of aggregates rather than single

* *Correspondence to: Richard Knochenmuss, Novartis Institutes for Biomedical Research, Tofwerk Uttigenstrasse 22, 3600 Thun, Switzerland. E-mail: rknochenmuss@gmx.net*

a *Novartis Institutes for Biomedical Research, Tofwerk Uttigenstrasse 22, 3600 Thun, Switzerland*

b *Department of Materials Science and Engineering, University of Virginia, 395 McCormick Road, Charlottesville, VA 22904-4745, USA*

molecules.[15,16] While any clusters or aggregates that can be mass analyzed or otherwise collected do not contribute directly to the desired signal of free, single ions, there have been suggestions that they play an important role in ion formation or release.[3,17–22]

MD simulations are an appropriate tool to gain insight into MALDI physics and chemistry. The main strength of the MD method is that only details of interatomic interactions need to be specified, and no assumptions are made about the nature of the complex processes triggered by the laser excitation. This is an important advantage that makes MD capable of discovering new physical phenomena or processes in the course of a 'computer experiment.' On the other hand, the limitations on the time and length scales accessible for MD simulations present a serious challenge for modeling of laser interactions with molecular systems. In order to expand the time and length scales in MD simulations and provide a description of laser excitation of a molecular system, a coarse-grained 'breathing sphere' MD model has been developed[23] and applied to investigation of the mechanism of laser desorption and ablation.[7–14]

A model combining the breathing sphere model designed for simulations of laser interactions with molecular systems and the ionization mechanisms described above[4–6] has been developed for MALDI.[24] This added considerably to the complexity and dynamics of energy conversion and deposition in the MALDI sample. While this model provided insights into the interplay of physical and chemical processes in MALDI, the initial results were limited to short simulation times, short laser pulses and did not include analyte molecules. Here we eliminate these limitations to better understand how laser pulse duration and fluence affect MALDI desorption/ablation and ionization over time scales allow better extrapolation to experimentally relevant observables.

Methods

The coarse-grained MD model of MALDI has been described previously.[24] Briefly, the breathing sphere model represents each matrix molecule as a sphere with one radial (breathing) degree of internal freedom.[7] This level of approximation allows modeling of large ensembles for experimentally relevant times. The photophysics and chemistry are the same as those included in the rate equation model,[4–6] as described above. The laser wavelength is taken here to be 355 nm. The excited matrix states include the S_1, at the energy of one laser photon (3.49 eV), and a higher excited state, S_n, at the energy of two photons. The reciprocal absorption coefficient of 350 nm corresponding to a cross section of 4×10^{18} cm^2 was used for S_0–S_1 excitation, and a twice larger cross section for S_1–S_n excitation. The ionization potential of matrix was taken to be that measured for DHB, 8.054 eV.[25]

Isotropic dipole–dipole interactions mediate hopping and pooling. A pooling ionization event yields a matrix cation and a free electron. The electron is propagated in a random direction, to be captured by neutral molecules at a rate determined by the cross section.[26–29] The mean free path in the solid matrix is thus on the order of 10 nm. Local, linearly density-dependent screening of electrostatic forces is included, the bulk dielectric constant was 30, decreasing to 1 for isolated ions.

Analytes are modeled with the 'bead-and-spring' model, where the 'beads' representing the building blocks of an oligomer molecule (monomers) are connected by anharmonic 'springs' with strengths appropriate for chemical bonding.[9,14] In this work, 40 oligomers of 10 units are included in some of the simulations. Each monomer is represented by a sphere, but with no internal degree of freedom. The mass of each monomer is the same as that of a matrix molecule (100 amu). The matrix–matrix and monomer–matrix non-covalent interactions are described by the same intermolecular interaction potential, parameterized to reproduce the van der Waals interaction in a typical molecular solid. The parameters of the 'springs' in the bead-and-spring model are chosen to represent covalent bonding along an oligomer chain. The functional form and parameters of the potential functions were as in reference [14]. An oligomer chain can break if the dissociation energy of any of the chemical bond within the chain is exceeded. In all of the MALDI simulations reported here the energy densities are insufficient to break any of the analyte oligomers.

A quenched, amorphous, matrix-only solid was the starting point for analyte incorporation. For each oligomer, initial monomers were randomly placed, subsequent members of the chain followed at random orientations (excluding those that cause overlap with prior monomers). The matrix molecules in the affected volume were removed, and the system again quenched until no further relaxation was observed.

Analyte molecules are treated as electronically inert, transparent to the laser radiation, unreactive in pooling, and do not trap excitons. Each monomer has the same electron capture cross section as matrix. Charge transfer reactions of monomers with matrix are an activated process. Every monomer has the same free energy of charge transfer reaction, but positive and negative charge transfer free energies are independently specified. The activation energy in either case was taken to be 25 kJ/mol, in both the forward and reverse directions.

The probability of a charge transfer event was calculated from the total energies of the system with and without the possible transfer. This included the total electrostatic energy, as well as the reaction energy. Calculation of the electrostatic energy includes periodic boundary conditions in the form of copies of the simulated volume in both lateral directions (3×3 arrangement). For a given ion (matrix or monomer) all possible transfers with nearby partners are calculated, and the probability of transfer with largest total energy decrease is evaluated, to determine if a transfer takes place.

The laser pulse was taken to have a Gaussian temporal profile, centered at a time after the start of the simulation corresponding to it's 1/e full width. The sample was uniformly irradiated, and no external electric fields were applied. The simulation time step was 5 fs if no analyte was included, and 2 fs otherwise. The initial MD computational systems had lateral (parallel to the surface) dimensions of 10 nm and a typical axial depth of 360 nm, including approximately 2.5×10^5 molecules. Below the MD computational cell a boundary condition was applied to minimize artificial reflection of pressure waves.[30] Periodic lateral boundary conditions were applied. For reasons of computational efficiency, the simulation volume is truncated at an arbitrary height above the irradiated surface, with molecules reaching the upper limit removed from the simulation. In this work a limit of 5000 nm was used.

Results

Plume properties

In reference [24], the MALDI event was simulated for less than 2 ns, a relatively short time compared to the hundreds of ns or more that are relevant for MALDI. To gain greater insight into the

Journal of MASS SPECTROMETRY

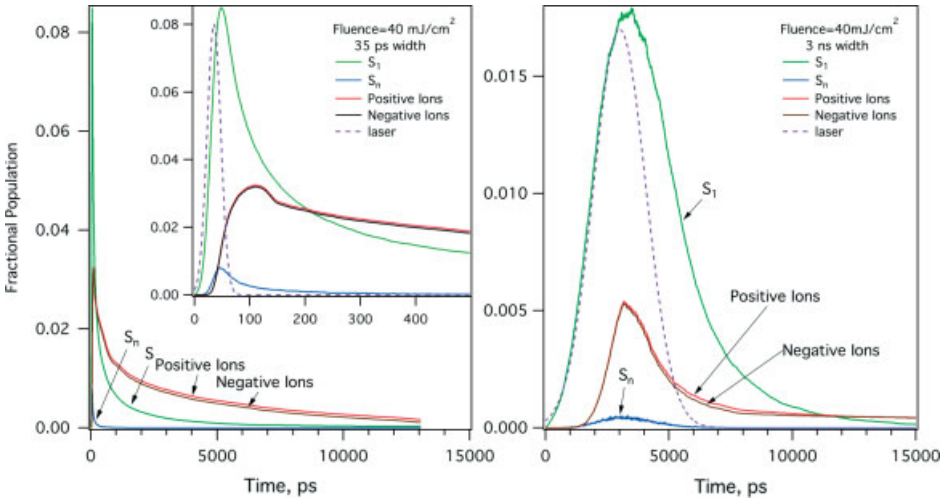

Figure 1. Evolution of matrix excited states and ions *versus* time, for 355-nm laser pulses of two different full widths: 35 ps and 3 ns, at a fluence of 40 mJ/cm^2. Ion formation and ablation are largely sequential for short pulse excitation, whereas they overlap considerably for the longer pulse length.

evolution of the plume, longer simulations were carried out as part of this study. Figure 1 shows the populations of the excited and ion states of matrix molecules for laser pulses that differ by almost two orders of magnitude in pulse width. The shorter pulse is similar to those reported in reference [24], and appropriate for a mode-locked picosecond Nd : YAG laser, while the longer one is more typical of Q-switched Nd : YAG lasers, which are often found in commercial MALDI instruments. Both simulations were carried out for a fluence which is moderately above the ion emission threshold, 40 mJ/cm^2.

Because the same energy is deposited in a shorter time, the excited state populations in the left panel reach significantly higher levels than in the right panel. The peak ion populations are also six times higher. For the short pulse, there is a clear ion formation period, to about $t = 100$ ps, corresponding to high S_1 and S_n populations. Recombination is initially slow, because migration of ions in the solid is very limited. Laser energy initially deposited in the form of S_1 excitations is gradually converted to heat by non-radiative decay, and melting begins at about $t = 130$ ps. Here 'melting' of the initially amorphous material is loosely used to describe the point at which ions become mobile in the condensed phase. Heating rapidly increases after melting, because the energy stored in ion pairs is released by recombination. This causes a distinct drop in the ion populations at about $t = 150$ ps. Note the significant delay in conversion of laser-deposited energy to heat compared to the duration of the laser pulse.

In spite of the stretched time scale, heating of the surface region is rapid enough to bring the liquid matrix up to the limit of thermodynamic stability with respect to spontaneous decomposition into vapor and liquid droplets (phase explosion).[31,32] This results in the explosive disintegration and ejection of a surface region of the irradiated target. The increasing mobility of ions in the expanding ablation plume provides opportunities for recombination, which continues for the whole duration of the simulation and results in a very small fraction of ions remaining in the plume at 13 ns. In the present model, recombination is believed to be unrealistically rapid at longer times because of the periodic boundary conditions. Lateral expansion of the plume is therefore not possible, which would quadratically reduce the pressure with distance downstream. The ion populations at long times are, therefore, presumably lower limits for what can be expected in MALDI events. Experimentally accessible ion yields will be discussed in more detail below.

Ion formation and material ejection are temporally less separated for the 3-ns laser pulse. Ion populations reach a maximum near the peak of the laser pulse, at about $t = 3$ ns. At this point melting and recombination reinforce each other, and ion concentrations drop quickly. Continued heating of the matrix creates the conditions for the onset of phase explosion at about $t = 4.5$ ns. This results in disintegration and ejection of a surface region. Similarly to the shorter pulse, the recombination of ions continues in the expanding plume, leading to a gradual flattening of the ion concentrations up to about 10 ns.

The density evolution of samples irradiated with 35, 350 and 3000 ps Gaussian pulses is shown in Fig. 2, all again at a fluence of 40 mJ/cm^2. The laser is incident from the right, along the Z axis. The material density is summed perpendicular to the plane of the figures, in layers parallel to the surface of the target. Because of the large difference in density between gaseous and condensed (generally liquid) phases, condensed ejecta are the most prominent features, appearing as curved dark tracks. The shortest pulse is characterized by the fewest such clusters and droplets of denser ablated material, as will be discussed in more quantitative detail below. However, both sub-nanosecond pulses cause spallation[8,12] of thick layers of colder material, from deep within the sample. This was also described in reference [24] for short pulses. Because a substantial fraction of incident laser energy is stored in excited states and the electrostatic energy of ions (see Fig. 1), the 35 ps pulse is not expected to be fundamentally different from the 350 ps pulse, which seems to be confirmed in Fig. 2.

These simulations are not long enough to define the ultimate ejection velocities, but the trajectories of the upper, faster aggregates are already rather linear in the upper right corners of the figure panels. This allows much better extrapolation of the plume behavior than the earlier, shorter simulations. The top cluster has an axial speed of about 700 m/s in all three cases. The slowest ions move at about 100 m/s for the longest pulse, though the deeper layers are still accelerating at the end of the simulation.

For the 350 ps pulse, it appears that the lowest velocities will also be about 100 m/s, although some acceleration in the deeper

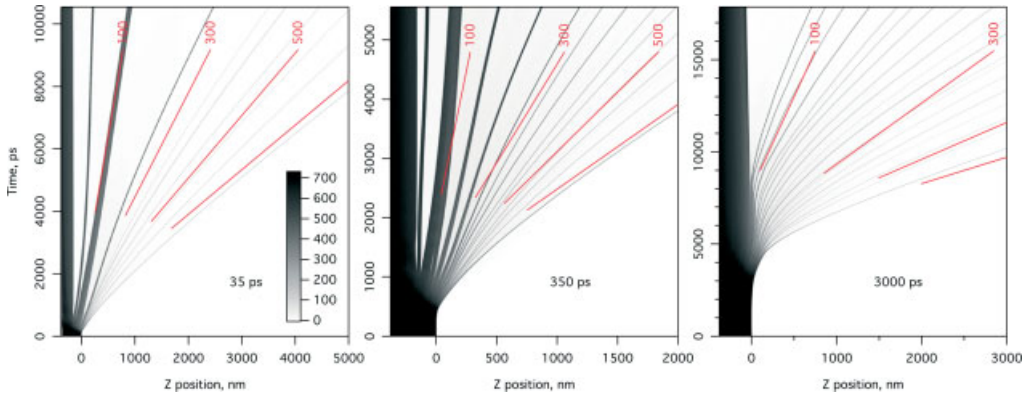

Figure 2. Laterally projected density *versus* time for samples irradiated with 40 mJ/cm^2, 355-nm laser pulses, of three different full widths: 35 ps, 350 ps and 3 ns. The laser is incident from the right, on the Z axis. The vertical axis has units of picoseconds. The density is in molecules per nm in the Z direction. The laser pulse is in each case centered at t = 1/e full width, or 350, 350 and 3000 ps. Lines representing velocities of 100, 300, 500, 700 and 900 m/s are plotted radiating from a single point or depth, for comparison to the trajectories of the ejected material.

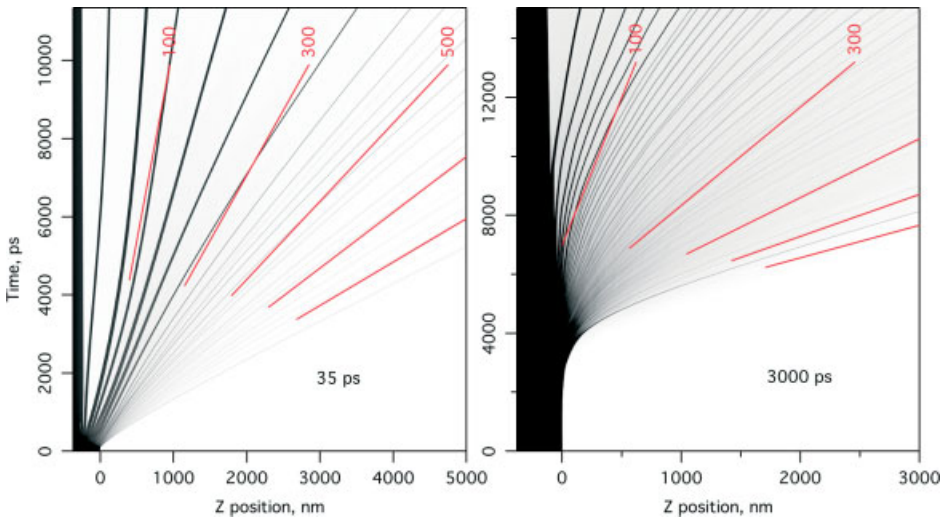

Figure 3. Laterally projected density *versus* time for samples irradiated with 50 mJ/cm^2, 355-nm laser pulses, of two different 1/e full widths: 35 ps, and 3 ns. The density scale is as in Fig. 2. Lines representing velocities of 100, 300, 500, 700 and 900 m/s are plotted radiating from a single point or depth, for comparison to the trajectories of the ejected material.

layers is still occurring at t = 5.5 ns. At the end of the simulation, the larger spalled layers are decelerating because of gas pressure above them. In the 35 ps case, the spallation layer has reached 100 m/s, most of the material is already faster at t = 10 ns.

Similar density plots are shown in Fig. 3 for short and long pulses, but at a higher fluence of 50 mJ/cm^2. Compared to the lower energy pulses, there are distinctly more, but smaller, clusters, dramatically so for the 3-ns laser pulse. In the case of the shorter pulse, the spalled layers are clearly decelerated at later times, reflecting the fact that the gas behind them is colder than the gas in front.

The velocities have been described in earlier simulations as a Maxwell distribution superimposed on a stream velocity distribution.[33,34] Lines representing a range of stream velocities are superimposed on Figs 2 and 3. In addition to aiding visualization of the velocities in the plume, they illustrate how velocities are strongly correlated with initial depth in the sample. The lines are plotted radiating from a single point, which was positioned to give a qualitative match to the near-asymptotic cluster trajectories. This virtual source is at the surface for short pulses, but deeper for longer pulses.

The strong correlation of the stream velocities with the initial depth in the sample is in similar to that found in earlier simulations which did not include MALDI-relevant energy deposition or storage mechanisms.[11,13,14,23,33,34] The virtual source depths were not identified earlier. The analyte molecules[23,33] and molecular clusters[10,14] are found to be entrained into the expanding plume and move along with the matrix molecules at approximately the same flow velocities. The large (non-thermal) spread in the axial velocities is consistent with the highly forward peaked angular distributions of ejected molecules observed in experiments[35,36] and in simulations[13,14], whereas entrainment of the analyte molecules and clusters in the plume can be related to the weak mass dependence of the ejection velocities and higher degree of forward peaking observed for analyte molecules in MALDI.[36–39]

An important aspect of the results shown in Figs 2 and 3 is that the velocity range of the ablated material is large, and changes with laser fluence (e.g. the fastest clusters move at about 700 m/s when ablated with 40 mJ/cm^2, but at about 900 m/s when ablated at 50 mJ/cm^2.) This is a straightforward consequence of the deposited energy density. More energy in a given volume results in higher temperature, pressure and subsequent forward

Journal of MASS SPECTROMETRY

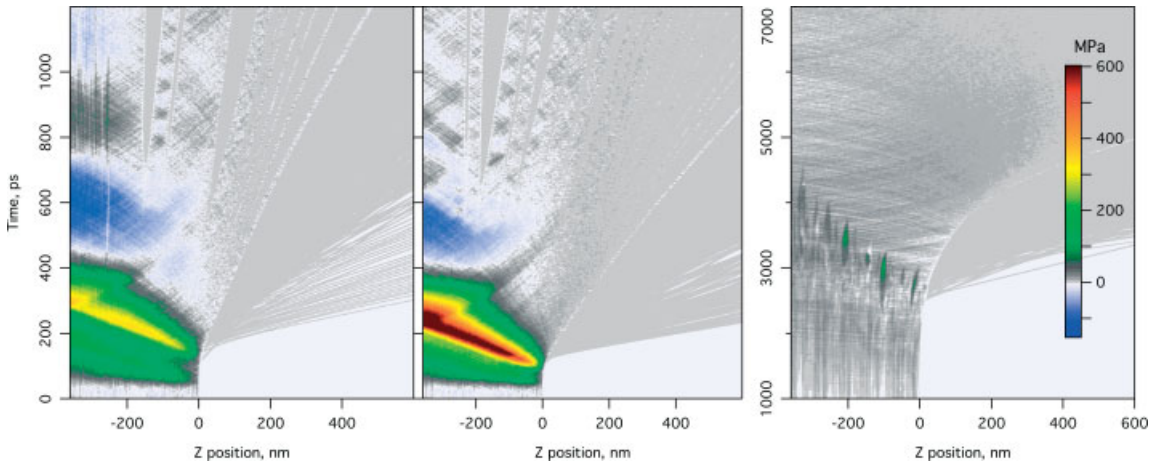

Figure 4. Laterally averaged pressure *versus* time, in Pascal. The left two panels show results for 35-ps laser pulse widths, of 40 (left) and 50 (middle) mJ/cm^2. The right panel shows results for a 3-ns, 50 mJ/cm^2 laser pulse. The color-coded pressure scale is the same for all panels.

velocity. For MALDI applications it is important to note that deposited energy density depends not only on the fluence, but on the matrix absorption coefficient at the laser wavelength. At a given wavelength, different matrixes may have a different absorption coefficient, which will result in different ablation velocities. Experimentally measured velocities will be discussed in more detail below.

Figure 4 shows the temporal development of pressure in the sample for different laser pulse characteristics. The shorter pulses result in much higher pressures than the longer one (stress confinement),[8,12,40], but the origin and shape of the pressure peak are highly dependent on concurrent photochemical processes. There is an initial weak pulse of compressive pressure during and shortly after the laser pulse, as non-radiative decay of S_1 states heats the sample. A second pulse follows, as the sample melts, allowing recombination to rapidly convert the stored energy of ion pairs to heat. This is very different from simulations not including ionization, where there are no such retardation effects in conversion of laser energy to heat.

In the left panel, the deposited energy is relatively low, and there is a distinct delay between the laser pulse itself (centered at $t =$ 35 ps), and the second pressure peak because of ion recombination energy release during melting, shortly before $t = 200$ ps. Because both the energy density and the rate of melting are highest near the surface, the pulse originates there, and propagates downward into the sample, passing the non-reflective boundary below the MD cell with only a slight reflection. The following rebound results in a substantial tensile unloading wave in the still dense material, which induces cavitation and spallation[8,12,40] at $Z = -175$ nm, and $t = 550$ ps. A residual elastic oscillation in the spalled material is attenuated within the simulated time frame.

In the 50 mJ/cm^2, 35 ps simulation, melting occurs sooner after the laser pulse, but weak direct heating is apparent before the very large release of thermal energy as a result of recombination. Although the peak pressure here is very high, the rebound wave is not more intense because the melt cannot support tensile stresses, and energy is dissipated either by cavitation or spallation. Similar decreases in tensile stress at higher fluence have been seen in other simulations.[12] Within less than 500 ps, the pressure has gone from peaks of $>6 \times 10^8$ Pa to $<1 \times 10^7$ Pa throughout.

The 3-ns laser pulse does not generate large pressure waves, since energy deposition, ion formation and melting all occur on a sufficiently extended time scale that stress confinement is not possible. The small areas of transiently higher pressures are regions where the initially amorphous material crystallized shortly before melting. At the end of the simulation, the pressures in the ejected material are in the same range as for the shorter laser pulses, in spite of quite different transient peak pressures, reflecting mechanical relaxation of the surface regions.

In Fig. 5 the density, pressure and temperature of the sample are shown at two times, for a 35 ps, 50 mJ/cm^2 laser pulse. Note that the temperature is calculated using only the lateral components of the velocities, so as not to be affected by the stream velocities. At $t = 1000$ ps, there are four distinct regions. Starting from the left, and extending to $Z = +200$ nm, are thick slabs, with low pressure gas in the gaps. These are the spallation products. In this zone, the temperature rises to the right, reflecting absorption of the excitation light *versus* depth.

From the peak of the temperature profile at $Z = 200$ to about $Z = 750$ nm is a region of decreasing density, pressure and temperature, containing many smaller clusters. This is the frothy material released by phase explosion. The material is thermally well equilibrated. The region is bounded by a relatively large cluster or droplet, and a sharp drop in pressure.

Above this surface is a purely gaseous region, where pressure and temperature decrease monotonically downstream as the material expands. Expansion cooling from the peak of about 1000 K down to about half that value is apparent. The decreasing density leads to increasingly large statistical fluctuations in the apparent values of temperature and pressure, above about $Z > 1100$ these values cannot be reliably defined and are not shown.

At $t = 11\,000$ ps, the material from the gaseous region has passed out of the simulation box to the right, as have many of the clusters. The entire remaining material is characterized by smoothly varying temperature and pressure, local equilibrium is approached. Regions further downstream are lower in pressure, because they expand faster. Pressures range from 0.5 to 1 MPa. The temperatures are around 700 K, with only slight differences between the condensed material and the surrounding gas.

In Fig. 6, early and late snapshots for a 3-ns laser pulse are shown. The $t = 5000$ ps snapshot is characterized by a smoothly decreasing density profile from the base of the melt to the surface of the leading cluster at $Z = 600$ nm. There is no spallation, this corresponds roughly to the cluster region of the 35 ps simulation.

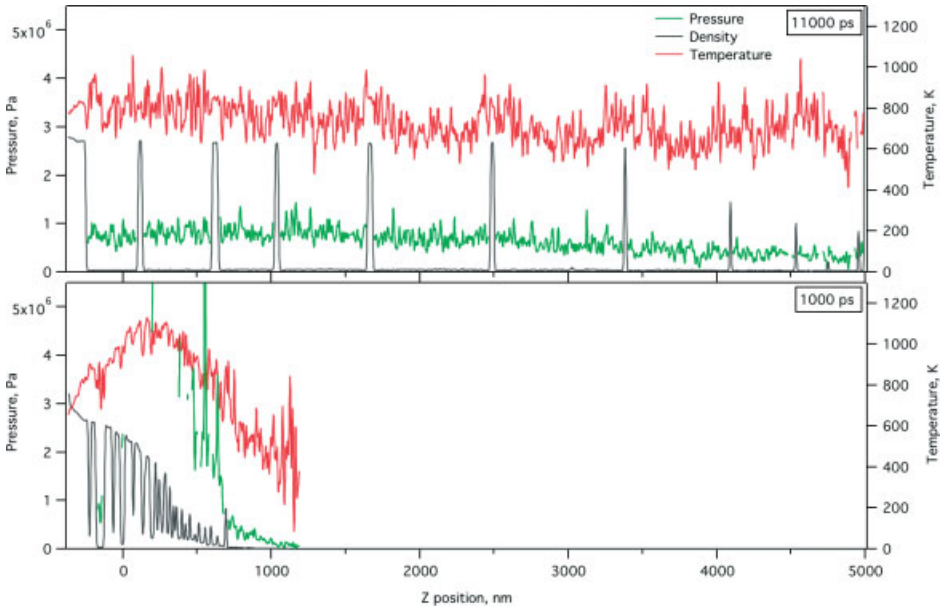

Figure 5. Snapshots of pressure, temperature and density *versus* axial distance for a 35 ps, 50 mJ/cm^2 laser pulse, at early and late times in the simulation. The pressure traces have been masked to show only the gaseous regions. The temperatures are calculated using only the lateral velocities, so as not to be distorted by the axial stream velocity. Regions of very low density, with too few molecules for a meaningful average, are also blanked.

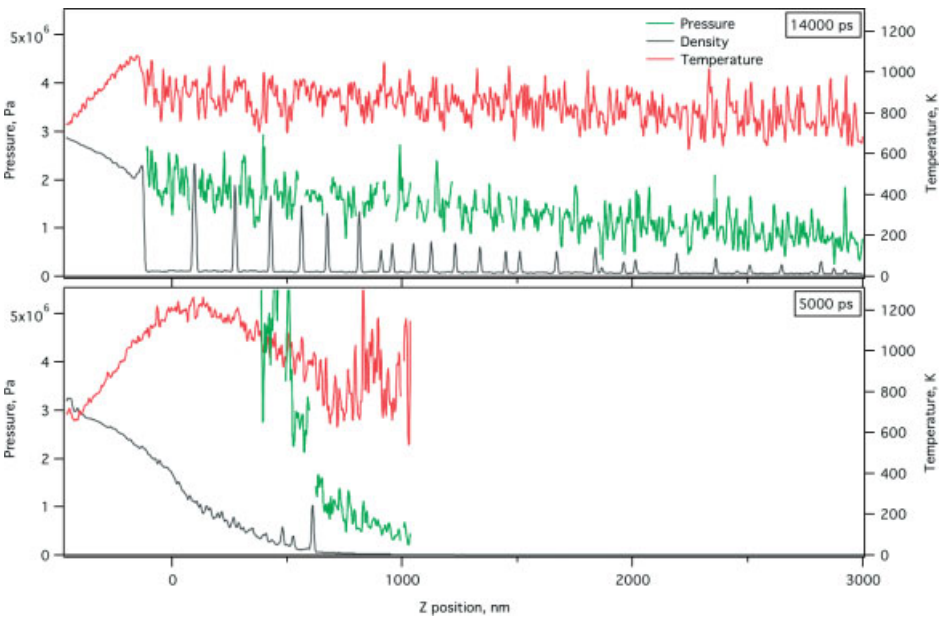

Figure 6. Snapshots of pressure, temperature and density *versus* axial distance for a 3-ns laser pulse, at early and late times in the simulation, at 50 mJ/cm^2. The pressure traces have been masked to show only the gaseous (low density) regions. The temperatures are calculated using only the lateral velocities, so as not to be distorted by the axial stream velocity. Regions of very low density, with too few molecules for a meaningful average, are also blanked.

The clusters tend, however, to be smaller. The pressure in the lower density parts of this region is relatively high compared to the desorbed gaseous region above the leading cluster. The temperature profile again exhibits a peak, below which it is characterized by the deposition profile, and above which it reflects expansion cooling.

In the gaseous region up to the leading cluster, temperature and density fall monotonically as a result of the rapid expansion. Although the low density further downstream is reflected in statistical temperature fluctuations, a generally elevated temperature from $Z = 600–1200$ nm is apparent. Similar increases of the radial temperature at the front of the expanding plume have been observed in earlier MD and Monte Carlo simulations of laser desorption/ablation[8,10,41] and have been attributed to the lack of equilibration in the low-density part of the plume.

At $t = 14\,000$ ps, clusters have emerged from the less differentiated froth, their sizes increase as a function of initial depth in the sample. The pressure decreases smoothly and slowly toward the right, as expected from a locally nearly equilibrated expansion. The temperature range is small, about 800 K.

Apart from the cold spalled chunks which carry few ions and are thus less important, the downstream differences between the

Journal of MASS SPECTROMETRY

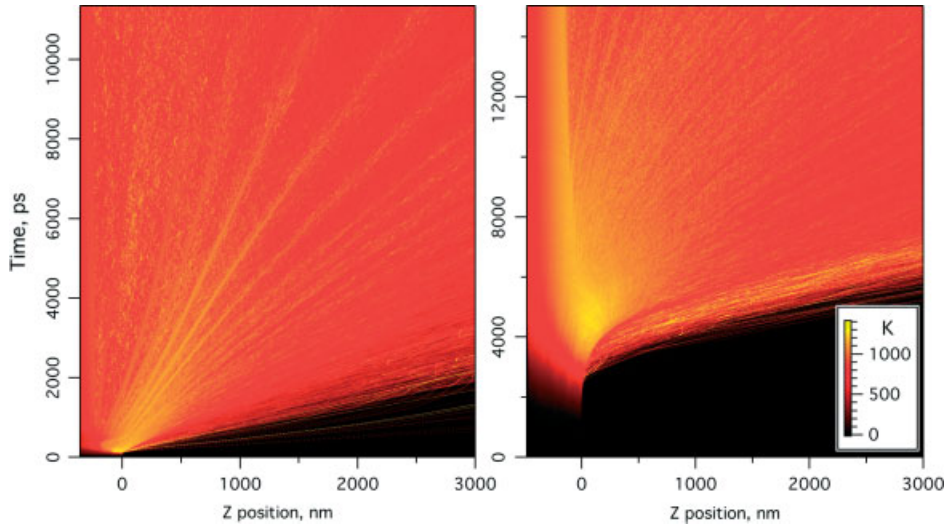

Figure 7. Laterally averaged temperature *versus* axial distance and time, for the simulations of Fig. 5 (left panel, 35-ps laser pulse) and Fig. 6 (right panel, 3-ns laser pulse).

short and long pulse events can be understood as differences between phase explosion (ns pulse width) and phase explosion assisted by pressure gradients because of stress confinement (ps pulse width).[8,10,40] In the latter case, the more rapidly ablated sample expands somewhat faster, which is reflected in a shorter period of high temperatures, and a lower final temperature for much of the material. This is illustrated in Fig. 7, showing the laterally averaged temperature *versus* downstream distance and time.

In the left panel of Fig. 7, it is apparent that the upper sample layers, initially the most highly energized, expand quickly and cool accordingly. Material from intermediate depths, the phase explosion region noted in Fig. 5, remains hotter for a longer time. Local equilibration with the gas between the clusters takes place over a few ns in this region. The clusters and droplets are visible at the top of Fig. 7, but this is due more to their density than temperature differences.

In contrast, the right panel exhibits regions that remain hot for a considerable time. Even after the clusters have emerged from the froth, expansion cooling takes more time than for the shorter pulse. In addition, deeper layers which were not ejected remain hot for a relatively long time, injecting energy into the gas behind the ablated material. The results of Figs 5, 6 and 7 suggest that the temperature evolution in the MALDI plume is defined not only by the laser fluence but also by the laser pulse width. Altough this observation is consistent with earlier ablation studies performed with 15 ps and 150 ps laser pulses,[8,10] it is somewhat surprising because the photophysics of energy deposition are different. As a result of the energy stored in excited states and significant ion concentrations, it might rather be expected that the laser pulse width is less important in a MALDI event than for ablation not including those phenomena, because conversion to thermal energy is always stretched out. However, as Fig. 1 shows, the stretching effect extends to a few 100 ps, so a nanosecond laser pulse is functionally substantially longer.

The role of clusters and aggregates in MALDI is a topic of current interest, and MD is especially helpful in addressing this issue. Figure 8 shows cluster histograms for the simulations of Figs 5–7. Both number density and mass-weighted number density are shown. The number density is the number of clusters in a size bin, normalized to the total number:

$$\text{Number Density} = 1/N_{\text{total}} \Sigma\, N(S)$$

where $N(S)$ is the number of clusters with size S, and the sum is between sizes S_{lower} and S_{upper} of each bin.

The mass-weighted density is the mass in a size bin, normalized to the total mass in the simulation:

$$\text{Mass Density} = 1/M_{\text{total}} \Sigma\, M(S)$$

where $M(S)$ is the total mass of all clusters of size S, and the sum is again between the limits of a histogram bin.

For both pulse lengths and at early times, single molecules are the most numerous species, making up at least 2/3 of all ejected particles. The number density of clusters larger than 10 molecules is negligible. A large mass fraction is also found in single molecules and clusters up to 100 molecules.

At long times, as the plume approaches local equilibrium, the size distribution has changed little, remaining dominated by $N < 10$. On the other hand, the mass fraction in larger clusters is significant. Clusters of 1000 molecules or more make up around half of the ejected mass, in both cases. For the 35 ps pulse, the largest clusters are the spallation droplets, which are larger than 10^4 molecules, while no similarly sized clusters are found for the longer pulse. Instead, a number of relatively large clusters have emerged from the explosive decomposition of the overheated matrix, in the $10^3 - 10^4$ size range. The short pulse produces fewer clusters between 10 and 1000 molecules than the long pulse.

Histograms are shown here rather than probability distribution functions, which have been used to characterize simulation results in other studies.[10,14] One reason for this is that some clusters escape the computational box at longer times, and are, therefore, no longer included in the calculations. As seen above, not all cluster sizes have the same speeds, (the largest ones are found only in the slower part of the plume), so a probability distribution function calculated at the same time points as the top panels of Fig. 8 would not be entirely accurate because of disproportionate loss of some cluster sizes from the box. This loss is less problematic in the linearly scaled histograms because it is found to affect

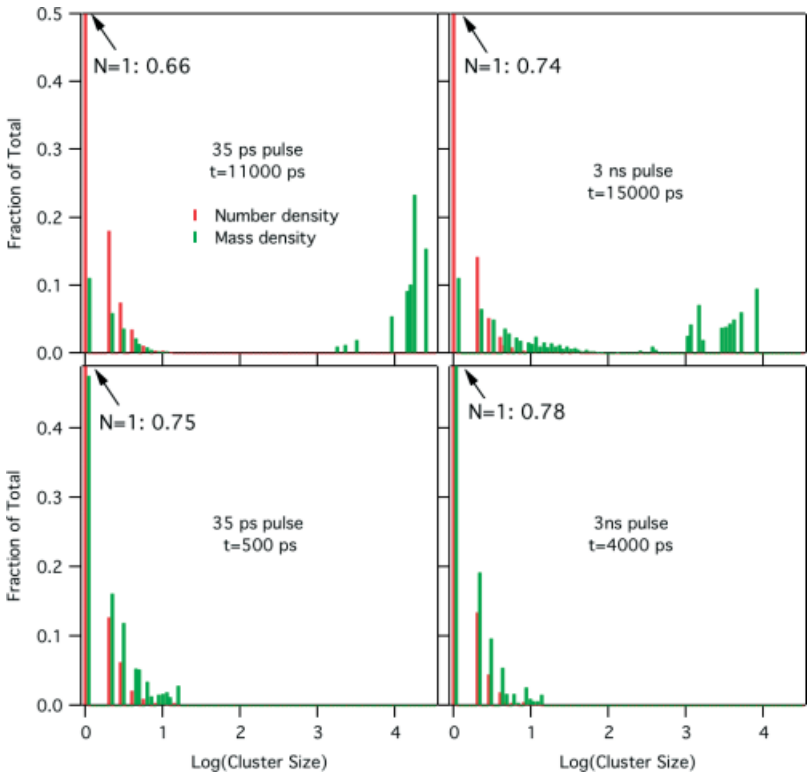

Figure 8. Normalized cluster number and mass-weighted histograms for short (35 ps) and long (3 ns) laser pulses, and early and late times. The fluence was 40 mJ/cm^2 in both cases. The mass-weighted histograms have been slightly laterally shifted for clarity.

mostly mid-size clusters. These are not numerous, nor do they carry a substantial fraction of the ablated mass.

Ionization

Having investigated the physical characteristics of the MALDI plume, we are now in a position to better understand factors influencing ion formation and release – the final objective of the MALDI process. Figure 9 shows the temporal and axial evolution of charge in the simulations of the preceding figures. Note that only matrix is present, no analyte ions are included.

As mentioned above, there is an initial build up of charge in the solid material, prior to melting. As a result of the higher S_1 and S_n electronic excitation densities generated by the short laser pulse, the ion density reaches peak values about three times higher than for the 3 ns pulse. As shown in reference [24], the S_n state is populated largely by exciton pooling (thereby depleting the S_1 population), even though the $S_n \leftarrow S_1$ transition has a considerably higher absorption cross section than the $S_1 \leftarrow S_0$.

In both cases, melting leads to rapid recombination, heating and the onset of the desorption/ablation processes already described. In addition, Fig. 9 makes apparent the early ejection of fast single ions from the surface layers, particularly for the short pulse. This effect was already described in reference [24]. A considerable number of fast ions are ejected on collisionless trajectories in the left panel. Because the surface charge is lower for the longer pulse, the first ions were mostly ejected as parts of the initial desorption/evaporation processes, and a few collisions with neutrals are evident in their trajectories.

In both panels, the intermediate velocity ions are entrained in a moderately dense, mostly molecular fluid, and undergo considerable numbers of collisions. Later ions are in an environment dominated by clusters and the gas between them. Many ions are carried in the clusters, but are also part of the equilibrium exchange of material with the gas. They are not bound to the clusters, but freely evaporate and condense. As seen in Fig. 10, matrix ions are distributed in about the same manner as the neutral material at both early and late times. There may be a slight enhancement in the intermediate size ranges at longer times.

The left panels of Fig. 11 show analyte polymers distributed in the matrix prior to irradiation and ablation by a 35 ps pulse. At $t = 250$ ps, well after irradiation is finished, the first matrix ions are ejected by the electric field which results from escape of electrons from the top few nm of the sample. These are all free ions, none are in clusters. Near the surface only positive analyte ions are found, consistent with the excess of positive charge there. In deeper layers, negatively charged analyte is also found, in roughly equal proportions. This reflects the ionization mechanism in the model, where an ionization event results in a matrix cation and a free electron. The electron may be captured by any molecule in the vicinity, including analyte.

At $t = 1000$ ps, the gas above the surface of the expanding froth ($Z > 350$ nm) entrains single matrix cations, and the upper region of the high density material ($Z = 150–350$ nm) is dominated by cations, both matrix and analyte. The lower part of this region, above the spalled layers ($Z = -100$ to 100 nm) has a more equal population of cations and anions. The total ion density is much less than at $t = 250$ ps, as recombination takes a heavy toll. There are no analyte anions, as the matrix acidity is higher than that of the analyte in this simulation.

At $t = 2000$ ps, there are well defined clusters, and the spallation droplets have clearly separated. In contrast to simulations with much longer polymers and higher polymer concentrations, there is

Journal of MASS SPECTROMETRY

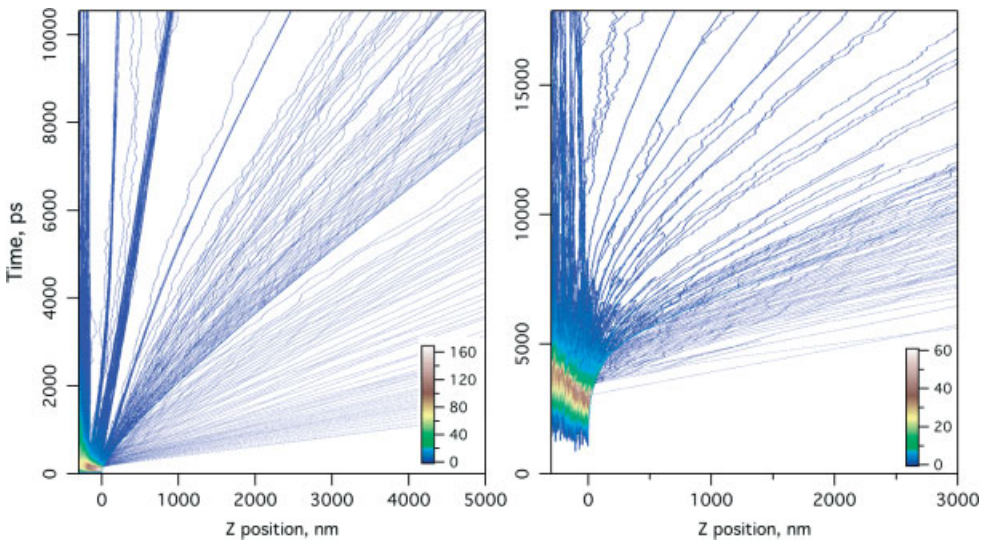

Figure 9. Laterally averaged charge density *versus* axial position and time, for the two simulations of Fig. 8. All charges are summed, positive and negative charges do not cancel. Note that the color scale spans different ranges for the two panels.

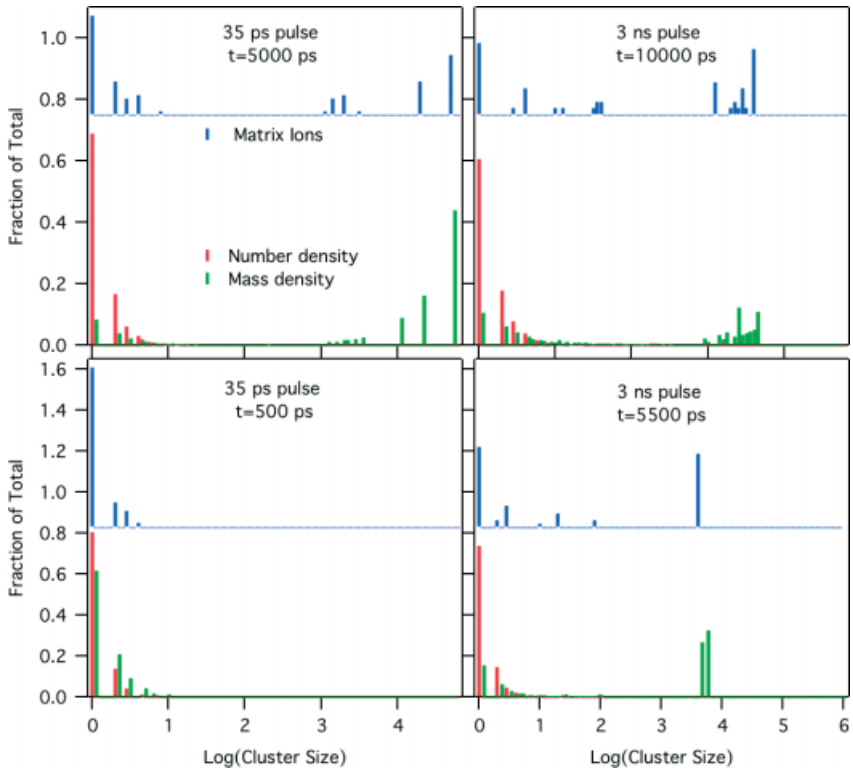

Figure 10. Normalized cluster size, mass and matrix ion histograms for short (35 ps) and long (3 ns) laser pulses, at early and late times. The fluence was 40 mJ/cm^2 in both cases. The ion histograms represent the masses of clusters in which one or more matrix ions are found. The mass-weighted histograms have been slightly laterally shifted for clarity.

no elongation of condensed material with entrained and oriented polymers.[14] The general features present at $t = 1000$ ps all remain, but are stretched in the axial direction. No analytes exist as free molecules, they are all embedded into clusters or droplets. The observation that analytes are always ejected parts of clusters of matrix molecules is consistent with other atomistic[42,43] and coarse-grained[9,14] simulations of matrix-assisted laser desorption. Analyte cannot evaporate from a cluster as the matrix molecules do because the net binding energy of a 10-mer is up to 10 times higher than that of a single matrix molecule. Free analyte ions are, therefore, expected to be released from clusters only under conditions where net matrix evaporation exceeds condensation.

The cluster embedding of analyte ions is seen more quantitatively in Fig. 12, for two time points. All analyte ions are found in the heavier end of the cluster histograms. There is little change in the proportion of larger clusters between the two time points. As noted above, major change in this respect will take considerable time and expansion.

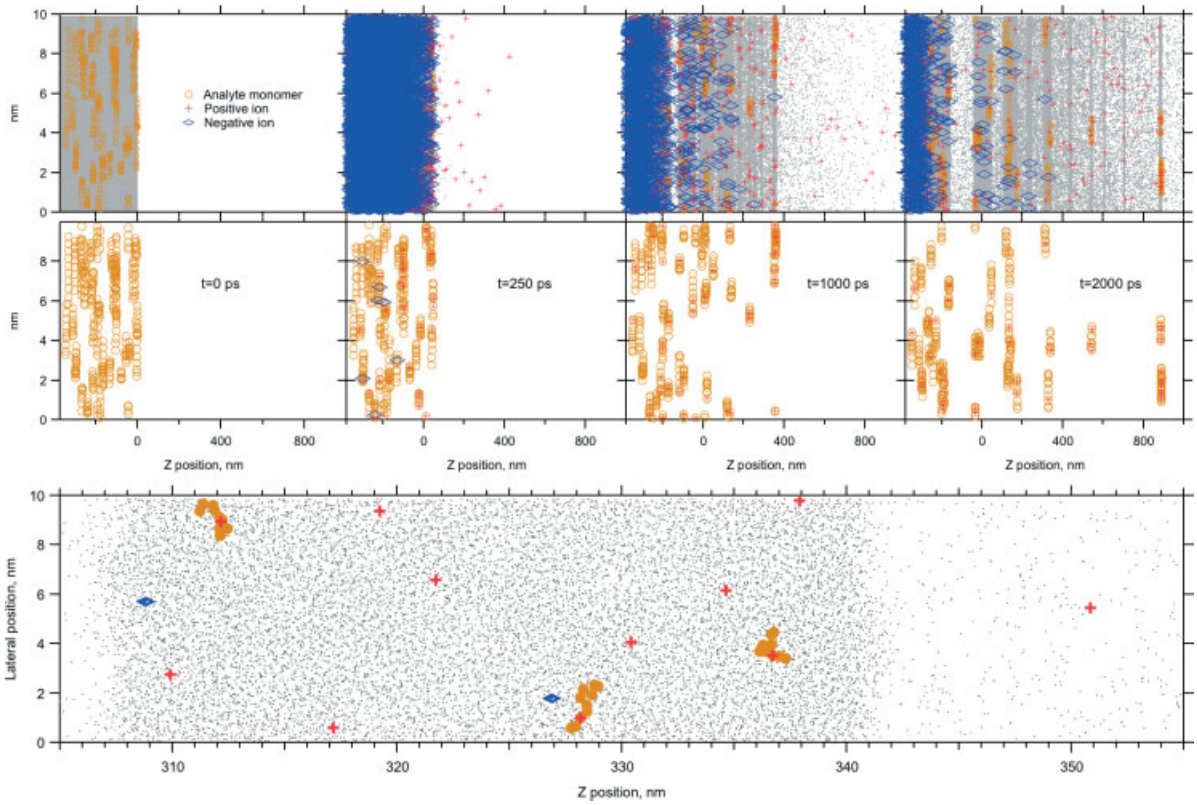

Figure 11. Snapshots of a simulation including 40 analyte polymers, each of 10 monomer units. The pulse width was 35 ps and the fluence was 40 mJ/cm^2. The top row of the top panel shows all molecules and ions. Neutral matrix is gray, positive ions red, negative ions blue. Analyte monomers are amber. The lower row shows only the analytes. Note that the vertical, lateral axis is much more expanded that the horizontal, axial one, causing the analytes to appear flattened. In fact, they are randomly oriented. The gas-phase basicity of each analyte monomer was taken to be 50 kJ/mol, making the overall polymer quite basic. As a result, several analytes become multiply positively charged, but none retains negative charge at longer times. The lower panel shows an expanded view of the rightmost time point in the top panel. The vertical and horizontal scales are the same. The random orientations of analytes in the liquid layer, and the irregular interface with the dense gas are apparent.

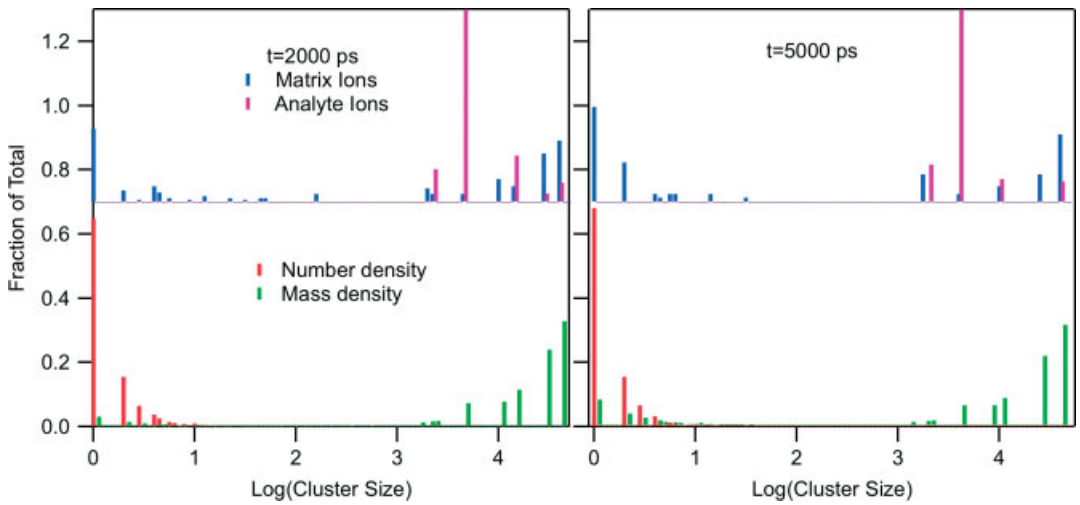

Figure 12. Histograms for the simulation of Fig. 11. Both matrix and analyte cluster ion histograms are shown, representing the sizes of the clusters in which ions are embedded. The mass-weighted and analyte ion histograms have been slightly laterally shifted for clarity.

Discussion

Experimentally, laser fluence has a larger influence on MALDI mass spectra than the irradiance.[44–48] The simulations presented here help understand why and to what extent that is the case. At a given fluence, the initial dynamics of the plume are noticeably different for short and long laser pulses. The high pressures and rapid early accelerations because of the short pulse, as well as the lack of overlap between excitation and expansion, lead initially to distinct regions of fast single molecules and ions, moderate sized clusters with dense gas between them, and spalled, large droplets. In contrast, the longer pulse is characterized by a more gradual

Journal of MASS SPECTROMETRY

and less differentiated transition. Pressures are far lower, clusters are initially smaller and more numerous, and no large aggregates are ejected. At later times, however, the differences are less pronounced. In both cases, clusters are entrained in a gas whose temperature and pressure at the end of these simulations are around 800 K, and $1-2\times10^6$ Pa, respectively. In the experimentally most useful part of the expansion that has high forward velocity, there are a few large clusters, of 1000 molecules or more, and the rest of size 10 or less.

The axial velocity ranges are also quite similar at the same fluence. The fastest clusters have axial speeds near 700 m/s at 40 mJ/cm^2, regardless of pulse length. These carry the first analyte ions available for analysis. At 50 mJ/cm^2, the speed of the earliest clusters is about 900 m/s, but is again independent of pulse width. The fan-like ejection pattern, with material radiating from a pseudo-source depth is also common to both long and short pulses. Ions are thoroughly entrained in the plume.

MALDI axial ion velocities have been repeatedly investigated, but the values reported span a remarkably large range, from a few 100 m/s to well over 1500 m/s.[20,36–39,49–61] Where velocity distributions were also measured, a similarly large range of distribution widths has also been reported.[37,38,51,61] The simulations suggest reasons why the experimental data has been so variable and inconclusive.

Time-of-flight (ToF) mass spectrometers typically focus ions originating in a limited region of time and space, so measurements have very likely sampled different parts of the plumes shown here. The early part contains a relatively high proportion of isolated matrix ions, which undergo few collisions. These ions are particularly amenable to ToF measurement, and a high mean ion velocity will be measured if they are selected. Deeper parts of the plume containing more analyte are subject to high collision rates for a considerable time, and analyte ions will apparently not be desolvated until far downstream. Adjusting the ion source to best extract these ions will result in measurement of distinctly lower mean velocities. In addition, analysis of ion arrival times has typically assumed that ions undergo no collisions and that external fields are not screened. Clearly these assumptions are not valid for large parts of the plume, and ion energy deficits corresponding to late ion release have been measured in detail.[56,57]

Without going into the complications arising from the numerous measurement and analysis methods used, the present results appear to be consistent with several ion velocity observations: the earliest matrix ions are faster than analyte ions, peak velocities increase somewhat with fluence, analyte ions may be entrained and/or be embedded in clusters for long periods after the laser pulse, and larger quantities of slower ions are generated at higher fluences.

Although temperatures found here in the later stages of the expansion are broadly consistent with experiment,[53,62–64] it is interesting to note that the plume equilibrates differently for short and long laser pulses. As seen in Fig. 7, the middle portion of the short pulse plume remains the hottest, with much of the thermal energy being carried in the bigger clusters. The top layers initially receive more deposited laser energy, but cool more quickly because they expand faster. This material is ejected with a moderate velocity, and the entrained ions should be extractable.

In contrast, the gradual acceleration of the long pulse plume results in a more extended region in time and space where the mid-layer material stays quite warm. In addition, not all of this warmer zone is ejected, and the remaining surface continues to evaporate at a relatively high rate, as seen in Fig. 3. This comparison suggests that shorter laser pulses may subject labile analytes to lower peak and integrated thermal loads. Analytes characterized by high activation energies for fragmentation may then undergo less decomposition. Because some matrix substances are known to be thermally labile as well,[65] their performance may also be affected by high sustained peak temperatures.

Because the ion formation processes in the present model are nonlinear, a short laser pulse generates many more primary ions than a long one, as seen in Fig. 9. This does lead to a higher yield of fast matrix ions at early times, but these are not analytically useful because no analyte is ejected at the same time. In the rest of the ejected material, ion recombination in the dense fluid is extensive. The few ions which are carried downstream are quite isolated from each other, as is evident in Fig. 11. Also in Fig. 9, it is clear that most of the ions are following separate trajectories, with only a few clusters containing multiple ions. The multiply charged analytes of Fig. 11 are an exception to this, but probably not a realistic one. Taking each monomer of the analyte to have the same high proton affinity is a simplification that needs to be revised.

The ions in these simulations which might go on to reach the detector of the mass spectrometer are, in a sense, 'lucky survivors' of the intense recombination period of the expansion. In contrast to the model of the same name,[3,17] however, these ions did not exist prior to laser excitation. Should any 'preformed' analyte ions initially be present, they would clearly be overwhelmed by the ion population formed by pooling processes. This modifies the discussion of MALDI ionization mechanisms somewhat – there need not be an 'either/or' choice. Preformed ions may exist in some cases in the form of analyte salts (not isolated ions), but if the pooling mechanism modeled here is active, they are irrelevant for the final ion yield.

The experimentally relevant ion yield cannot be uniquely defined in these simulations. Because the spatial and temporal extent of a real MALDI event cannot be molecularly simulated for practical reasons, it is not clear which of the ions in the figures would finally be usable in a mass spectrometer. Certainly the early, fast matrix ions are detectable, they are well-adapted to ToF mass spectrometers, or any ion extraction/manipulation technique. The later ions, which must be desolvated and reach a reasonably low density before being extracted, are more problematic.

If the regions which have a forward velocity greater than about 100 m/s are integrated, the yield in the results shown here is about 5×10^{-4} (ions : neutrals), consistent with experimental estimates.[44,48,66–70] Any instrumental limitation of the extent to which the plume is sampled, in time, space or velocity, will correspondingly reduce the yield.

In present form, the model yields too many highly charged analyte ions. Setting this aside for the moment, Fig. 11 shows a secondary analyte ion yield of about 50% in the rightmost frame. In other words, about half the ions present are analyte ions. Secondary charge transfer reactions are efficient, thanks to the early high matrix ion concentration and the many collisions in the early plume. In this simulation, there are many more matrix ions than analyte can react with (although not all analytes are ionized in the last panel of Fig. 11), so the ratio will not change much downstream. Were analyte present at substantially higher concentration, or fewer primary ions created by a lower fluence laser pulse, the matrix ion population could be depleted further. This matrix suppression effect is predicted by the rate equation model, and is observed in practice,[5,71–73] but further simulations

with higher analyte concentrations will be needed to investigate it at a molecular level.

The role of clusters in MALDI ionization, particularly of analytes, remains a point of active discussion. Experimental evidence for entrainment, late ion release and analyte embedding in clusters has been available for some time,[56,57,74] and cluster-based models followed soon after.[3,17] Massive clusters of analyte ions with matrix have been suggested, up to 50 000 Da and more,[18] and various pathways for their decay into observable analyte ions suggested.[9,19–22]

Although more extensive simulations are needed to better understand the role of clusters in MALDI, the current results are quite consistent with analyte entrainment in large clusters early in the plume.[9,14,42,43] As Fig. 12 shows, both short and long laser pulses lead to clusters of matrix with analyte that have total masses of at least 1000 matrix molecules. In the current model the matrix has mass 100 Da, and the analyte 1000. The clusters are, therefore, of total mass $>1 \times 10^5$ Da. Some of these are early in the plume, and thus in some sense 'prompt,' but all are far behind the fastest matrix ions which are released from very near the initial surface. Because no free analytes are found here, the question of single or dual kinetic domains for analyte ion formation cannot yet be addressed.[56,57] How clustering and desolvation depend on analyte size also remains to be investigated.

As the plume continues to expand beyond the time range considered here, it is currently unclear whether complete evaporation can be expected within the present model. As analyte ions are, in fact, released in MALDI, such a result would suggest the model is incomplete. Mechanisms for addition of energy downstream might include acceleration of charged clusters by the extraction electric field, or reactions such as asymmetric electron transfer.[75]

Conclusions

MD simulations of MALDI, including both physical and chemical processes, were carried out to investigate the role of laser pulse width and fluence on primary and secondary ionization process.

While 35-ps laser pulses led to a relatively stratified early plume, long pulses of 3 ns result in smoother transitions between regimes of molecular and cluster ablation. Short pulses lead to much higher initial pressures and ion concentrations in the condensed phase, but these differences rapidly decay as a result of the phase change. This is in accordance with experiment.

Peak axial velocities in the plume are somewhat fluence dependent, and span a very wide range. The earliest matrix ions have high velocities, but clusters containing analytes are no faster than 700 m/s at 40 mJ/cm^2 and 900 m/s at 50 mJ/cm^2. At the end of the simulations presented here, the trajectories of the bulk of the ejected material are as if they were originating from a single depth. This depth is near the original surface for shorter pulses, and somewhat below that surface for longer pulses. This may be useful in design of better ion extraction optics.

It does not appear to be meaningful to speak of MALDI matrix substances as having characteristic ablation velocities. Rather, it seems that the dramatic inconsistencies between measurements of various types and in different labs are more likely a consequence of instrumental and experimental design factors, which select different parts of the plume for analysis. At the same time, several qualitative aspects of velocity measurements are confirmed by the simulations, such as relative matrix: analyte velocities, and shifts with fluence.

Consistent with experiment, fast matrix cations are ejected in a near-collisionless regime before slower entrained matrix and analyte ions are accelerated downstream. The total ion yield is 5×10^4 or less, depending on what regions of the plume are assumed to finally reach the detector. This is in the same range as experimental estimates. Secondary reaction of matrix cations with analyte neutrals was efficient in these simulations, reflecting the favorable thermodynamics. Analyte ions remained entrained in large clusters of matrix throughout the simulations. This is consistent with a variety of experimental evidence, but it remains unclear how and at what rate these ions are desolvated. This will be the object of forthcoming studies.

The transient ion population in the pooling model is much larger than that which could be present in the form of preformed analyte ions. Any preformed ions are, therefore, largely irrelevant to the evolution of the ion populations and the final ion yield.

Acknowledgements

One of the authors (L. V. Z.) acknowledges financial support from the National Science Foundation (Award CMMI-0800786). The authors would like to thank Elodie Leveugle for assistance with setting up the model for analyte molecules.

References

[1] R. Knochenmuss. Ion formation mechanisms in UV-MALDI. *The Analyst* **2006**, *131*, 966.
[2] K. Dreisewerd. The Desorption Process in MALDI. *Chem. Rev.* **2003**, *103*, 395.
[3] M. Karas, R. Krueger. Ion Formation in MALDI: the cluster ionization mechanism. *Chem. Rev.* **2003**, *103*, 427.
[4] R. Knochenmuss. A Quantitative Model of Ultraviolet Matrix-assisted Laser Desorption and Ionization. *J. Mass Spectrom.* **2002**, *37*, 867.
[5] R. Knochenmuss. A Quantitative Model of UV-MALDI Including Analyte Ion Generation. *Anal. Chem.* **2003**, *75*, 2199.
[6] R. Knochenmuss. A bipolar rate equation model of MALDI primary and secondary ionization processes, with application to positive/negative analyte ion rations and suppression effects. *Int. J. Mass Spectrom.* **2009**, *285*, 105.
[7] L. V. Zhigilei, P. B. S. Kodali, B. J. Garrison. A Microscopic View of Laser Ablation. *J. Phys. Chem. B* **1998**, *102*, 2845.
[8] L. V. Zhigilei, B. J. Garrison. Microscopic mechanism of laser ablation of organic solids in the thermal stress confinement irradiation regime. *J. Appl. Phys.* **2000**, *88*, 1.
[9] T. E. Itina, L. V. Zhigilei, B. J. Garrison. Microscopic Mechanisms of Matrix Assisted Laser Desorption of Analyte Molecules: Insights from Molecular Dynamics Simulation. *J. Phys. Chem. B* **2002**, *106*, 303.
[10] L. V. Zhigilei. Dynamics of the plume formation and parameters of the ejected clusters in short-pulse ablation. *Appl. Phys. A* **2003**, *76*, 339.
[11] L. V. Zhigilei, E. Leveugle, B. J. Garrison, Y. G. Yingling, M. I. Zeifman. Computer Simulations of Laser Ablation of Molecular Substrates. *Chem. Rev.* **2003**, *103*, 321.
[12] E. Leveugle, D. S. Ivanov, L. V. Zhigilei. Photomechanical spallation of molecular and metal targets: molecular dynamics study. *Appl. Phys. A* **2004**, *79*, 1643.
[13] L. V. Zhigilei, Y. G. Yingling, T. E. Itina, T. A. Schoolcraft, B. J. Garrison. Molecular dynamics simulation soft matrix-assisted laser desorption-connections to experiment. *Int. J. Mass Spectrom.* **2003**, *226*, 85.
[14] E. Leveugle, L. V. Zhigilei. Molecular dynamics simulation study of the ejection and transport of polymer molecules in matrix-assisted pulsed laser evaporation. *J. Appl. Phys.* **2007**, *102*, 074914.
[15] M. Handschuh, S. Nettesheim, R. Zenobi. Laser-Induced Molecular Desorption and Particle Ejection from Organic Films. *Appl. Surf. Sci.* **1998**, *137*, 125.

[16] S. N. Jackson, S. Mishra, K. K. Murray. Characterization of Coarse Particles Formed by Laser Ablation of MALDI Matrixes. *J. Phys. Chem. B* **2003**, *107*, 13106.
[17] M. Karas, M. Glückmann, J. Schäfer. Ionization in MALDI: singly charged molecular ions are the lucky survivors. *J. Mass Spectrom.* **2000**, *35*, 1.
[18] I. Fournier, C. Marinach, J.-C. Tabet, G. Bolbach. Irradiation effects in MALDI, ablation, ion production and surface modifications. Part II: 2,5-dihydroxybenzoic acid monocrystals. *J. Am. Soc. Mass Spectrom.* **2003**, *14*, 893.
[19] S. Alves, I. Fournier, C. Afonso, F. Wind, J.-C. Tabet. Gas-phase ionization/desolvation processes and their effect on protein charge state distributions under MALDI conditions. *Eur. J. Mass Spectrom.* **2006**, *12*, 369.
[20] I. Fournier, A. Brunot, J.-C. Tabet, G. Bolbach. Delayed extraction experiments using a repulsive potential before ion extraction: evidence of clusters as ion precursors in UV-MALDI. Part I: dynamical effects with the matrix 2,5-dihydroxybenzoic acid. *Int. J. Mass Spectrom.* **2002**, *213*, 203.
[21] I. Fournier, A. Brunot, J.-C. Tabet, G. Bolbach. Delayed extraction experiments using a repulsive potential before ion extraction: evidence of non-covalent clusters as ion precursors in UV MALDI. Part II-dynamic effects with alpha-cyano-4-hydroxycinnamic acid matrix. *J. Mass Spectrom.* **2005**, *40*, 50.
[22] E. Sachon, G. Clodic, T. Blasco, G. Bolbach. Protein Desolvation in UV Matrix-Assisted Laser Desorption/Ionization (MALDI). *J. Am. Soc. Mass Spectrom.* **2007**, *18*, 1880.
[23] L. V. Zhigilei, P. B. S. Kodali, B. J. Garrison. Molecular Dynamics Model for Laser Ablation and Desorption of Organic Solids. *J. Phys. Chem. B* **1997**, *101*, 2028.
[24] R. Knochenmuss, L. V. Zhigilei. A molecular dynamics model of UV-MALDI including ionization processes. *J. Phys. Chem. B* **2005**, *109*, 22947.
[25] V. Karbach, R. Knochenmuss. Do Single Matrix Molecules Generate Primary Ions in Ultraviolet Matrix-Assisted Laser Desorption/Ionization? *Rapid Commun. Mass Spectrom.* **1998**, *12*, 968.
[26] S. A. Pshenichnyuk, N. L. Asfandiarov. The role of free electrons in MALDI: electron capture by molecules of alpha-cyano-4-hydroxycinnamic acid. *Eur. J. Mass Spectrom.* **2004**, *10*, 477.
[27] S. A. Pshenichnyuk, N. L. Asfandiarov, V. S. Fal'ko, V. G. Lukin. Temperature dependence of dissociative electron attachment to molecules of gentisic acid, hydroquinone and p-benzoquinone. *Int. J. Mass Spectrom.* **2003**, *227*, 281.
[28] S. A. Pshenichnyuk, N. L. Asfandiarov, V. S. Fal'ko, V. G. Lukin. Temperature dependencies of negative ion formation by capture of low-energy electrons for some typical MALDI matrices. *Int. J. Mass Spectrom.* **2003**, *227*, 259.
[29] N. L. Asfandiarov, S. A. Pshenichnyuk, A. I. Forkin, V. G. Lukin, V. S. Fal'ko. Electron capture negative ion mass spectra of some typical MALDI matrices. *Rapid Commun. Mass Spectrom.* **2002**, *16*, 1760.
[30] L. V. Zhigilei, B. J. Garrison. Pressure waves in microscopic simulations of laser ablation. *J. Mat. Res. Soc. Symp. Proc.* **1999**, *538*, 491.
[31] A. Miotello, R. Kelly. Laser-induced phase explosion: the new physical problems when a condensed phase approaches the thermodynamic critical temperature. *Appl. Phys. A* **1999**, *69*, S676.
[32] B. J. Garrison, T. E. Itina, L. V. Zhigilei. The limit of overheating and the threshold behavior in laser ablation. *Phys. Rev. E* **2003**, *68*, 41501.
[33] L. V. Zhigilei, B. J. Garrison. Velocity Distributions of Analyte Molecules in Matrix-Assisted Laser Desorption from Computer Simulations. *Rapid Comm. Mass Spectrom.* **1998**, *12*, 1273.
[34] L. V. Zhigilei, B. J. Garrison. Velocity Distributions of Molecules Ejected in Laser Ablation. *Appl. Phys. Lett.* **1997**, *71*, 551.
[35] J. W. Elam, D. H. Levy. Laser Ablation of Trp-Gly. *J. Phys. Chem. B* **1998**, *102*, 8113.
[36] W. Z. Zhang, B. T. Chait. Radial Velocity Distributions of Molecular Ions Produced by Matrix-Assisted Laser Desorption/Ionization. *Int. J. Mass Spectrom. Ion Proc.* **1997**, *160*, 259.
[37] T. Huth-Fehre, C. H. Becker. Energetics of Gramicidin S after UV Laser Desorption from a Ferrulic Acid Matrix. *Rapid Commun. Mass Spectrom.* **1991**, *5*, 378.
[38] Y. Pan, R. J. Cotter. Measurement of the Initial Translational Energies of Peptide Ions in Laser Desorption/Ionization Mass Spectrometry. *Org. Mass Spectrom.* **1992**, *27*, 3.
[39] S. Berkenkamp, C. Menzel, F. Hillenkamp, K. Dreisewerd. Measurements of Mean Initial Velocities of Analyte and Matrix Ions in Infrared Matrix-Assisted Laser Desorption Ionization Mass Spectrometry. *J. Am. Soc. Mass Spectrom.* **2002**, *13*, 209.
[40] L. V. Zhigilei, B. J. Garrison. Mechanisms of laser ablation from molecular dynamics simulations: dependence on the initial temperature and pulse duration. *Appl. Phys. A* **1999**, *69*, S75.
[41] S. Sibold, H. M. Urbassek. Kinetic Study of pulsed desorption flows into vacuum. *Phys. Rev. A* **1991**, *43*, 6722.
[42] M. Sadeghi, X. Wu, A. Vertes. Conformation Changes, Complexation and Phase Transition in Matrix-Assisted Laser Desorption. *J. Phys. Chem. B* **2001**, *105*, 2578.
[43] Y. Dou, N. Winograd, B. J. Garrison, L. V. Zhigilei. Substrate-Assisted Laser-Initiated Ejection of Proteins Embedded in Water Films. *J. Phys. Chem. B* **2003**, *107*, 2362.
[44] R. C. Beavis. Phenomenological Models for Matrix-assisted Laser Desorption Ion Yields Near the Threshold Fluence. *Org. Mass Spectrom.* **1992**, *27*, 864.
[45] R. E. Johnson. Models for Matrix-Assisted Desorption by a Laser-Pulse. *Int. J. Mass Spectrom. Ion Proc.* **1994**, *139*, 25.
[46] P. Demirev, A. Westman, C. T. Reimann, P. Håkansson, D. Barofsky, B. U. R. Sundqvist, Y. D. Cheng, W. Seibt, K. Siegbahn. Matrix-Assisted Laser Desorption with Ultra-Short Laser Pulses. *Rapid Commun. Mass Spectrom.* **1992**, *6*, 187.
[47] K. Dreisewerd, M. Schürenberg, M. Karas, F. Hillenkamp. Matrix-Assisted Laser Desorption/Ionization with Nitrogen Lasers of Different Pulse Widths. *Int. J. Mass Spectrom. Ion Proc.* **1996**, *154*, 171.
[48] K. Riahi, G. Bolbach, A. Brunot, F. Breton, M. Spiro, J.-C. Blais. Influence of Laser Focusing in Matrix-assisted Laser Desorption/Ionization. *Rapid Commun. Mass Spectrom.* **1994**, *8*, 242.
[49] R. C. Beavis, B. T. Chait. Velocity Distibutions of Intact High Mass Polypeptide Molecule Ions Produced by Matrix-Assisted Laser Desorpion. *Chem. Phys. Lett.* **1991**, *181*, 479.
[50] J. Zhou, W. Ens, K. G. Standing, A. Verentchikov. Kinetic Energy Measurement of Molecular Ions Ejected into an Electric Field by Matrix-Assisted Laser Desorption. *Rapid Commun. Mass Spectrom.* **1992**, *6*, 671.
[51] C.-W. Chou, R. W. Nelson, P. Williams. Dependence of the ejection velocities of laser-ablated ions on the laser wavelength and fluence. *Eur. J. Mass Spectrom.* **2009**, *15*, 305.
[52] B. Spengler, D. Kirsch. On the formation of initial ion velocities in matrix-assisted laser desorption ionization: Virtual desorption time as an additional parameter describing ion ejection dynamics. *Int. J. Mass Spectrom.* **2002**, *226*, 71.
[53] T. W. Jaskolla, M. Karas, U. Roth, K. Steinert, C. Menzel, K. Reihs. Comparison Between Vacuum Sublimed and Conventional Dried Droplet Preparation in MALDI-TOF Mass Spectrometry. *J. Am. Soc. Mass Spectrom.* **2009**, *20*, 1104.
[54] M. Karas, U. Bahr, I. Fournier, M. Glückmann, A. Pfenninger. The initial-ion velocity as a marker for different desorption-ionization mechanisms in MALDI. *Int. J. Mass Spectrom.* **2003**, *226*, 239.
[55] P. Juhasz, M. L. Vestal, S. A. Martin. On the Initial Velocity of Ions Generated by Matrix-Assisted Laser-Desorption/Ionization and Its Effect on the Calibration of Delayed Extraction Time-of-Flight Mass-Spectra. *J. Am. Soc. Mass Spectrom.* **1997**, *8*, 209.
[56] G. R. Kinsel, M. E. Gimon-Kinsel, K. J. Gillig, D. H. Russell. Investigation of the Dynamics of Matrx-assisted Laser Desorption/Ionization Ion Formation Using an Electrostatic Analyzer/Time-of-flight Mass Spectrometer. *J. Mass Spectrom.* **1999**, *34*, 684.
[57] G. R. Kinsel, R. D. Edmondson, D. H. Russell. Profile and Flight Time Analysis of Bovine Insulin Clusters as a Probe of Matrix-Assisted Laser Desorption/Ionization Ion Formation Dynamics. *J. Mass Spectrom.* **1997**, *32*, 714.
[58] V. Livadaris, J.-C. Blais, J.-C. Tabet. Formation of non-specfic protein cluster ions in MALDI: abundances and dynamical aspects. *Eur. J. Mass Spectrom.* **2000**, *6*, 409.
[59] M. Glüeckmann, M. Karas. The Initial Ion Velocity and Its Dependence on Matrix, Analyte and Preparation Method in Ultraviolet Matrix-assisted Laser Desorption/Ionization. *J. Mass Spectrom.* **1999**, *34*, 467.
[60] B. Spengler, V. Böekelmann. Angular and Time-Resolved Intensity Distributions of Laser-Desorbed Matrix Ions. *Nucl. Instr. Meth. Phys. Res. B* **1993**, *82*, 379.

[61] V. Böekelmann, B. Spengler, R. Kaufmann. Dynamical Parameters of Ion Ejection and Ion Formation in Matrix-Assisted Laser Desorption/Ionization. *Eur. Mass Spectrom.* **1995**, *1*, 81.
[62] G. Luo, I. Marginean, A. Vertes. Internal energy of ions generated by MALDI. *Anal. Chem.* **2002**, *74*, 6185.
[63] V. Gabelica. E. Schulz, M. Karas. Internal energy build-up in MALDI. *J. Mass Spectrom.* **2004**, *39*, 579.
[64] J. H. Moon, S. H. Yoon, M. S. Kim. Temperature of Peptide Ions Generated by Matrix-Assisted Laser Desorption Ionization and Their Dissociation Kinetic Parameters. *J. Phys. Chem. B* **2009**, *113*, 2071.
[65] O. I. Tarzi, H. Nonami, R. Erra-Balsells. The effect of temperature on the stability of compounds used as UV-MALDI-MS matrix: 2,5 DHB, 2,4,6 THAP, CHCA, 35, dimethoxy-4-hydroxycinnamic acid, nor-harmane and harmane. *J. Mass Spectrom.* **2009**, *44*, 260.
[66] A. A. Puretzky, D. B. Geohegan. Gas-phase Diagnostics and LIF Imaging of 3-hydroxypicolinic acid MALDI Matrix Plumes. *Chem. Phys. Lett.* **1997**, *286*, 425.
[67] K. Dreisewerd, M. Schürenberg, M. Karas, F. Hillenkamp. Influence of the Laser Intensity and Spot Size on the Desorption of Molecules and Ions in Matrix-Assisted Laser-Desorption/Ionization with a Uniform Beam Profile. *Int. J. Mass Spectrom. Ion Proc.* **1995**, *141*, 127.
[68] C. Mowry, M. Johnston. Simultaneous Detection of Ions and Neutrals Produced by Matrix-assisted Laser Desorption. *Rapid Comm. Mass Spectrom.* **1993**, *7*, 569.
[69] A. P. Quist, T. Huth-Fehre, B. U. R. Sundqvist. Total Yield Measurements in Matrix-Assisted Laser Desorption Using a Quartz Crystal Microbalance. *Rapid Commun. Mass Spectrom.* **1994**, *8*, 149.
[70] W. Ens, Y. Mao, F. Mayer, K. G. Standing. Properties of Matrix-Assisted Laser Desorption. Measurements with a Time-to-Digital Converter. *Rapid Commun. Mass Spectrom.* **1991**, *5*, 117.
[71] R. Knochenmuss, V. Karbach, U. Wiesli, K. Breuker, R. Zenobi. The Matrix Suppression Effect in Matrix-Assisted Laser Desorption/Ionization: Application to Negative Ions and Further Characteristics. *Rapid Commun. Mass Spectrom.* **1998**, *12*, 529.
[72] R. Knochenmuss, F. Dubois, M. J. Dale, R. Zenobi. The Matrix Suppression Effect and Ionization Mechanisms in Matrix-Assisted Laser Desorption/Ionization. *Rapid Commun. Mass Spectrom.* **1996**, *10*, 871.
[73] A. J. Hoteling, W. F. Nichols, D. J. Giesen, J. R. Lenhard, R. Knochenmuss. Electron transfer reactions in LDI and MALDI: factors influencing matrix and analyte ion intensities. *Eur. J. Mass Spectrom.* **2006**, *12*, 345.
[74] A. N. Krutchinsky, B. T. Chait. On the nature of chemical noise in MALDI mass spectra. *J. Am. Soc. Mass Spectrom.* **2002**, *13*, 129.
[75] G. Kinsel, R. Knochenmuss, P. Setz, C. M. Land, S.-K. Goh, E. F. Archibong, J. H. Hardesty, D. Marynick. Ionization energy reductions in small 2,5-dihydroxybenzoic acid-proline clusters. *J. Mass Spectrom.* **2002**, *37*, 1131.